JAEA-Research
2006-089

JAEA-Research

Kinetic Simulations of Electrostatic Plasma Waves using Cubic-Interpolated-Propagation Scheme

Maxime LESUR*, Yasuhiro IDOMURA
and Shinji TOKUDA

Center for Computational Science & e-systems

January 2007

Japan Atomic Energy Agency

日本原子力研究開発機構

本レポートは日本原子力研究開発機構が不定期に発行する成果報告書です。
本レポートの入手並びに著作権利用に関するお問い合わせは、下記あてにお問い合わせ下さい。
なお、本レポートの全文は日本原子力研究開発機構ホームページ（http://www.jaea.go.jp/index.shtml）より発信されています。このほか財団法人原子力弘済会資料センター*では実費による複写頒布を行っております。

〒319-1195　茨城県那珂郡東海村白方白根2番地4
日本原子力研究開発機構　研究技術情報部　研究技術情報課
電話 029-282-6387, Fax 029-282-5920

*〒319-1195　茨城県那珂郡東海村白方白根2番地4　日本原子力研究開発機構内

This report is issued irregularly by Japan Atomic Energy Agency
Inquiries about availability and/or copyright of this report should be addressed to
Intellectual Resources Section, Intellectual Resources Department,
Japan Atomic Energy Agency
2-4 Shirakata Shirane, Tokai-mura, Naka-gun, Ibaraki-ken 319-1195 Japan
Tel +81-29-282-6387, Fax +81-29-282-5920

Kinetic Simulations of Electrostatic Plasma Waves using Cubic-Interpolated-Propagation Scheme

Maxime LESUR*, Yasuhiro IDOMURA+ and Shinji TOKUDA+

Center for Computational Science & E-systems
Japan Atomic Energy Agency
Tokai-mura,Naka-gun,Ibaraki-ken

(Received December4,2006)

Kinetic properties of small amplitude waves in an electron plasma are studied using analytic and numerical calculations based on the Vlasov-Poisson system. The dispersion relation of plasma waves in a Maxwellian plasma is solved using Laplace-Fourier transform, and it is shown that waves decay in time by Landau damping. A simulation code for solving the Vlasov-Poisson system in phase space is developed using the Cubic-Interpolated-Propagation (CIP) scheme, and Landau damping is successfully calculated numerically. Finally, the stability of an electron plasma with a beam component is discussed by applying these analytic and numerical approaches.

Keywords: Plasma Waves,Vlasov Simulation, CIP Scheme, Landau Damping, Gentle-bump Instability

*Ecole Polytechnique,France
+Fusion Research and Development Directorate

CIP法を用いた静電的プラズマ波の運動論的シミュレーション

日本原子力研究開発機構システム計算科学センター
Maxime LESUR*, 井戸村　泰宏+, 徳田　伸二+

(平成18年12月　4日 受理)

電子プラズマにおける小振幅波動の運動論的特性をVlasov-Poisson方程式系に基づく解析計算および数値計算によって調べた.Maxwellianプラズマにおけるプラズマ波の分散関係をLaplace-Fourier変換によって解析し,プラズマ波がLandau減衰によって減衰することを示した.Vlasov-Poisson方程式系を位相空間において解き進めるシミュレーションコードをCIP法を用いて開発しLandau減衰の数値計算に成功した.これらの解析的および数値的手法を適用してビーム成分を伴う電子プラズマの安定性を議論した.

原子力科学研究所（駐在）〒319-1195 茨城県那珂郡東海村白方白根2-4

*Ecole Polytechnique, France

+核融合研究開発部門

Contents

目 次

1 INTRODUCTION

In a high temperature fusion plasma, typical density and temperature parameters are respectively given as $n \sim 10^{14}\mathrm{cm}^{-3}$ and $T \sim 1\mathrm{keV}$, which lead to the collision frequency ν much smaller than the plasma frequency ω_0, $\nu \ll \omega_0$. Therefore, a fusion plasma is deviated from a local thermodynamic equilibrium, and kinetic properties become distinct. In principle, its kinetic behaviours may be fully described by the Newton-Maxwell system. However, such a primitive approach is too heavy to be computed, and we introduce a statistical approach based on a particle distribution function. A collisionless model without multiple body correlations or particle collisions is a good approximation of a high temperature fusion plasma. In this work, we use the collisionless Vlasov-Poisson system to study kinetic properties of an electron plasma with electrostatic perturbations.

One of the most basic kinetic properties of a collisionless plasma is collisionless damping of a perturbed particle distribution. Even without collisional dissipation, free streaming of particles produces damping by phase mixing. In addition, if one consider self-consistent perturbations, resonant interactions between waves and particles lead to the Landau damping. In this work, we study these phenomena in an one-dimensional (1D) electron plasma, which is the simplest model for understanding these phenomena, and solve the 1D Vlasov-Poisson system using analytic and numerical approaches. Although an analytic method to solve the linear Vlasov-Maxwell system was established by Landau [1], a numerical simulation of the Vlasov-Maxwell system often has difficulties because of the following points. Firstly, we need to capture small amplitude fluctuations, which are typically less than $\sim 1\%$ of the equilibrium density in a fusion plasma. Secondly, we are interested in so-called normal modes, which are weakly damped (or growing) waves. The Landau theory tells us that the damping rate γ becomes very small compared to the real frequency ω_r, where the phase velocity ω_r/k_x is in the tail of particle distribution. An accurate treatment of such weak wave-particle interaction is required to get a small damping rate with $\gamma/\omega_r \leq 1\%$. In this study, we adopt the Cubic-Interpolated-Propagation (CIP) scheme [2], which is one of the modern Computational Fluid Dynamics (CFD) schemes, and develop a Vlasov CIP code, which simulate the 1D Vlasov-Poisson system in phase space. We show linear comparisons of numerical results with the Landau theory, and then, apply the simulation to a problem of the inverse Landau damping or an instability in an electron plasma with a beam component.

The reminder of the paper is organised as follows. In Sec.2, the 1D Vlasov-Poisson system is solved to obtain the dispersion relation using Fourier-Laplace transform, and the theory of Landau damping is reviewed. In Sec.3, numerical methods used in the Vlasov CIP code are presented, and numerical properties such as numerical oscillations and the recurrence effect are studied. In Sec.4, Landau damping is simulated using the Vlasov CIP code, and a dispersion relation obtained numerically is compared to analytic results to check the physical validity of the simulation. In Sec.5, as an application of these analytic and numerical approaches, the gentle-bump instability is analysed. Finally, a summary is given in Sec. 6.

2 LANDAU DAMPING

2.1 Linearised Vlasov-Poisson system

We study the propagation of small amplitude plasma waves through an uniform electron plasma with no equilibrium magnetic field. Let $f(\vec{r},\vec{v},t)$ be the particle distribution function, where $\vec{r}$ and $\vec{v}$ are the position and the velocity of a particle, respectively. We consider the Vlasov-Poisson system [3] as a starting point.

$$\frac{\partial f}{\partial t} + (\vec{v}\cdot\vec{\nabla})f + \frac{e}{m}\vec{\nabla}\varphi\cdot\vec{\nabla}_v f = 0, \tag{1}$$

$$-\vec{\nabla}^2\varphi = 4\pi e\left[n_0 - \int f\,d\vec{v}^{\,3}\right], \tag{2}$$

where e and m are the elementary charge and the electron mass, in "cgs" units, φ is the electrostatic potential, n is the electron density, and n_0 is the neutralising ion density.

As we consider small amplitude waves, we linearise Eqs. (1) and (2) by separating the total distribution function f into an equilibrium part f_0 and a perturbed part δf, respectively,

$$f(\vec{r},\vec{v},t) = f_0(\vec{v}) + \delta f(\vec{r},\vec{v},t). \tag{3}$$

By assuming the quasi-neutrality condition, $n_0 = \int f_0 d\vec{v}^{\,3}$, we have a set of linearised equations,

$$\frac{\partial \delta f}{\partial t} + (\vec{v}\cdot\vec{\nabla})\delta f + \frac{e}{m}\vec{\nabla}\varphi\cdot\vec{\nabla}_v f_0 = 0, \tag{4}$$

$$-\vec{\nabla}^2\varphi = -4\pi e\int \delta f d\vec{v}^{\,3}, \tag{5}$$

We then solve the linearised Vlasov-Poisson system for the initial condition $\delta f(\vec{r},\vec{v},0) = g(\vec{r},\vec{v})$, and determine the resulting perturbations.

2.2 Analytic expression of electrostatic potential

As Eqs. (4) and (5) are linear and do not depend on the coordinate system explicitly, a function $\delta f(\vec{r},\vec{v},t)$ can be expanded into a Fourier integral with respect to arbitrary coordinates,

$$f_k(\vec{v},t) = \frac{1}{(2\pi)^3}\int_{-\infty}^{\infty}\delta f(\vec{r},\vec{v},t)e^{-\imath\vec{k}\vec{r}}\,d\vec{r}, \tag{6}$$

$$\varphi_k(t) = \frac{1}{(2\pi)^3}\int_{-\infty}^{\infty}\varphi(\vec{r},t)e^{-\imath\vec{k}\vec{r}}\,d\vec{r}, \tag{7}$$

$$g_k(\vec{v}) = \frac{1}{(2\pi)^3}\int_{-\infty}^{\infty}g(\vec{r},\vec{v})e^{-\imath\vec{k}\vec{r}}\,d\vec{r}. \tag{8}$$

Here, we consider a certain wave vector $\vec{k}$ and take the x axis along $\vec{k} = k_x\vec{x}$. By applying the Fourier transform, Eqs. (4) and (5) yield a new equation system in Fourier space,

$$\frac{\partial f_k}{\partial t} + \imath k v_x f_k + \imath k_x\frac{e}{m}\varphi_k\frac{\partial f_0}{\partial \vec{v}_x} = 0, \tag{9}$$

$$k_x^2\varphi_k = -4\pi e\int f_k\,d\vec{v}^{\,3}. \tag{10}$$

We then apply Laplace transform in time,

$$f_p(\vec{v}) = \int_0^{\infty} f_k(\vec{v},t)e^{-pt}\,dt, \tag{11}$$

$$\varphi_p = \int_0^{\infty}\varphi_k(t)e^{-pt}\,dt. \tag{12}$$

When the growth of $f_k(\vec{v},t)$ is slower than an exponential dependence $e^{\sigma t}$, $f_p(\vec{v})$ is defined for $\mathfrak{Re}(p) \geq \sigma > 0$. In the inverse Laplace transform, we perform the integration in the complex p-plane along a straight line parallel to the imaginary axis and passing to the right of it,

$$f_k(\vec{v},t) = \frac{1}{2\pi\imath}\int_{-\imath\infty+\sigma}^{\imath\infty+\sigma} f_p(\vec{v})e^{pt}\,dp, \tag{13}$$

$$\varphi_k(t) = \frac{1}{2\pi\imath}\int_{-\imath\infty+\sigma}^{\imath\infty+\sigma}\varphi_p e^{pt}\,dp. \tag{14}$$

By taking the Laplace transform, Eqs. (9) and (10) yield

$$(p + \imath k_x v_x) f_p(\vec{v}) + \imath k_x \frac{e}{m} \varphi_p \frac{\partial f_0(\vec{v})}{\partial \vec{v}_x} = g_k(\vec{v}), \tag{15}$$

$$k_x^2 \varphi_p = -4\pi e \int f_p(\vec{v})\, \vec{dv}^3. \tag{16}$$

Eliminating f_p in the last two equations gives an expression for φ_p,

$$\varphi_p = -\frac{4\pi e}{k_x^2} \frac{\int \frac{g_k(\vec{v})}{p + \imath k_x v_x} \vec{dv}^3}{1 - \frac{4\pi \imath e^2}{k_x m} \int \frac{\partial f_0(\vec{v})}{\partial \vec{v}_x} \frac{\vec{dv}^3}{p + \imath k_x v_x}}. \tag{17}$$

By performing integration over v_y and v_z, Eq. (17) can be reduced as

$$\varphi_p = -\frac{4\pi e}{k_x^2} \frac{N(p)}{D(p)} \tag{18}$$

$$N(p) = \int_{-\infty}^{\infty} \frac{g(u)}{p + \imath k_x u}\, du, \tag{19}$$

$$D(p) = 1 - \frac{4\pi \imath e^2}{k_x m} \int_{-\infty}^{\infty} \frac{\partial f_0(u)}{\partial u} \frac{du}{p + \imath k_x u}, \tag{20}$$

where $u \equiv v_x$, $g(u) = \int g_k(\vec{v}) dv_y dv_z$, and $f_0(u) = \int f_0(\vec{v}) dv_y dv_z$.

2.3 Time asymptotic solution of plasma waves

To determine $\varphi(t)$ in the asymptotic limit or $t \to \infty$, we take the inverse Laplace transform of φ_p. This complex integral can be easily performed if we displace the integral path to $\mathfrak{Re}(p) < \sigma$. For this purpose, we need φ_p for $p \in \mathbb{C}$. Although φ_p is defined only for $\mathfrak{Re}(p) > \sigma$, we can extend the definition of φ_p in the whole complex p-plane by the analytic continuation [4].

If one suppose that $g(u)$ is analytic on the whole complex u plane, the only singularity of $N(p)$ is $u = \imath p/k_x$. According to the Cauchy's theorem, the following relation holds for the cases represented in Fig.1,

$$\oint_C \frac{g(u)}{p + \imath k_x u} du = \frac{2\pi}{k_x} g\left(\frac{\imath p}{k_x}\right) \tag{21}$$

In the limit of $R \to \infty$, the integration along the big semi-circle will vanish. Consequently, the redefined $N(p)$ using modified integral paths P in Fig.2, $N(p) = \int_P g(u)/(p + \imath k_x u) du$, is the analytic continuation of the original $N(p)$, and this function has no singularity at

finite values of p. The same discussion is applicable also to $D(p)$, provided that $df_0(u)/du$ is an entire function on the whole complex-u plane. Therefore, the only singularities of φ_p are the zeros of $D(p)$.

In the inverse Laplace integration formula (14), the integration is performed over the Bromwitch path B_p represented in Fig.3. However, the Cauchy's theorem tells us that the integration along the closed path $B_1 + B_2 + B_3 + B_4$ is zero. Moreover, if we take the limit of $h \to \infty$, the integration along B_2 and B_4 will vanish, which gives $\int_{B_1} = -\int_{B_3}$. Therefore, we can displace the integration path from B_p to D_p with going around all the poles of φ_p. Let p_k be the pole of $D(p)$, which is the nearest to the imaginary axis. In the inverse Laplace transform, $\varphi_k(t) = \int_{D_p} \varphi_p e^{pt} dt/(2\pi\imath)$, only the residue related to p_k is of importance for large values of t, because of the presence of the factor e^{pt}. Thus, the electrostatic potential $\varphi(t)$ is proportional to $e^{p_k t}$. If we write $p_k = -\imath\omega = -\imath\omega_r - \gamma$, $e^{-\imath\omega_r t - \gamma t}$ shows a wave with the damping rate γ and the real frequency ω_r. Here, p_k is determined by the dispersion relation,

$$D(p) = 1 - \frac{4\pi\imath e^2}{k_x m} \int_P \frac{\partial f_0(u)}{\partial u} \frac{du}{p + \imath k_x u} = 0. \tag{22}$$

2.4 Limiting case of long waves

In the small k_x limit, a resonance point given by $u = \imath p/k_x$ goes to large $|u|$, where the particle distribution becomes very small. This leads to weak wave-particle interaction, and therefore, we may assume a small damping rate, $\gamma \ll \omega_r$. By applying this assumption, we expand $D(\omega)$ around $\omega \sim \omega_r$,

$$D(\omega) \approx D(\omega_r) - \imath\gamma \frac{\partial}{\partial \omega_r} D(\omega_r). \tag{23}$$

We then solve $D(\omega) = 0$ to obtain ω_r and γ,

$$\mathfrak{Re}(D(\omega_r)) = 0, \tag{24}$$

$$\gamma = \frac{\mathfrak{Im}(D(\omega_r))}{\partial \mathfrak{Re}(D(\omega_r))/\partial \omega_r}, \tag{25}$$

where $D(\omega_r)$ is given as

$$D(\omega_r) = 1 - \frac{\omega_0^2}{k_x^2 n_0} \mathcal{P} \int \frac{\partial f_0/\partial u}{u - \omega_r/k_x} du - \pi\imath \frac{\omega_0^2}{k_x^2 n_0} \left. \frac{\partial f_0}{\partial u} \right|_{u=\omega_r/k_x}. \tag{26}$$

In Eq. (26), the second term shows the Cauchy's principal value, and the third term gives an imaginary part. For a Maxwellian plasma,

$$f_0(u) = n_0\sqrt{\frac{m}{2\pi\kappa T}}e^{-\frac{mu^2}{2\kappa T}}, \tag{27}$$

Eq. (24) yields

$$\begin{aligned}\mathfrak{Re}(D(\omega_r)) &= 1+\frac{1}{\sqrt{\pi}k_x^2\lambda_D^2}\mathcal{P}\int\frac{ve^{-v^2}}{v-\xi}dv \\ &= 1-\frac{1}{2k_x^2\lambda_D^2}Z'(\xi) \\ &= 0,\end{aligned} \tag{28}$$

where $\xi = \omega_r/(\sqrt{2}k_x v_{th})$, $v = u/(\sqrt{2}v_{th})$, v_{th} is the electron thermal velocity, κ is the Boltzmann constant, $\lambda_D = \sqrt{\kappa T/(4\pi ne^2)}$ is the Debye length, and

$$Z(\xi) \equiv \frac{1}{\sqrt{\pi}}\int_{-\infty}^{\infty}\frac{e^{-v^2}}{v-\xi}dv. \tag{29}$$

For the long wavelength limit considered here, Eq. (29) can be approximated by asymptotic expansion for $|\xi| \gg 1$ [3],

$$Z(\xi) \sim -\frac{1}{\xi}-\frac{1}{2\xi^3}-\frac{3}{4\xi^5}-\cdots. \tag{30}$$

Finally, we have the dispersion relation,

$$1-\frac{\omega_0^2}{\omega_r^2}-3k_x^2\lambda_D^2\frac{\omega_0^4}{\omega_r^4} = 0, \tag{31}$$

where the plasma frequency is defined as $\omega_0^2 = 4\pi n_0 e^2/m$. The dispersion relation (31) gives the k_x-dependence of ω_r as

$$\begin{aligned}\omega_r &= \pm\sqrt{\frac{1}{2}\omega_0\left(1+\sqrt{1+12k_x^2\lambda_D^2}\right)} \\ &\simeq \pm\omega_0\left(1+\frac{3}{2}\lambda_D^2k_x^2\right).\end{aligned} \tag{32}$$

The group velocity, $\partial\omega_r/\partial k_x = (3/2)\lambda_D^2\omega_0 k_x$, is not constant but proportional to k_x. Consequently, any initial perturbation consisting of multiple k_x components will be distorted as it propagates.

By substituting ω_r to Eq. (25), γ is obtained as

$$\gamma \sim -\frac{\pi}{2n_0}\frac{\omega_r^3}{k_x^2}\frac{\partial f_0}{\partial u}\bigg|_{u=\omega_r/k_x} \tag{33}$$

In Eq. (33), we see that the damping rate γ is given by $\partial f_0/\partial u$ at the velocity $u = \omega_r/k_x$. A final expression of γ for a Maxwellian plasma is given as

$$\gamma(\omega_r) \sim \sqrt{\frac{\pi}{8}} \frac{\omega_r^4}{k_x^3 \lambda_D^3 \omega_0^3} \exp\left[-\frac{\omega_r^2}{2k_x^2 \lambda_D^2 \omega_0^2}\right]. \tag{34}$$

3 NUMERICAL METHODS

3.1 Normalised equation system

From here, we discuss the 1D Vlasov-Poisson system with the particle distribution $f(x, v_x, t)$, which is obtained by integrating Eqs. (1) and (2) over v_y and v_z.

$$\partial_t f + v_x \partial_x f + \frac{e}{m} \partial_x \varphi \partial_v f = 0, \tag{35}$$

$$-\partial_x^2 \varphi = 4\pi e \left[n_0 - \int f dv_x\right], \tag{36}$$

In a typical fusion plasma with $n_0 \sim 10^{14}\mathrm{cm}^{-3}$ and $T \sim 1\mathrm{keV}$, characteristic spatio-temporal scales are given by $\omega_0^{-1} \sim 10^{-11}\mathrm{s}$ and $\lambda_D \sim 10^{-4}\mathrm{cm}$. To avoid treatments of too big and too small numbers in a numerical simulation, it is useful to normalise an equation system by the above characteristic scales. In addition, results from such a normalised equation system are applicable to a plasma with arbitrary plasma parameters, provided that assumptions used are valid for those parameters. In the normalisation, we choose the units of time, length, charge, mass, and density as ω_0^{-1}, λ_D, e, m, and n_0, respectively. If we denote the original quantities with an hat ($\hat{t}$, $\hat{x}$, $\hat{f}$...), and the normalised dimensionless quantities without hat (t, x, f...), they are related as $t = \omega_0 \hat{t}$, $x = \lambda_D^{-1}\hat{x}$, $v_x = (\lambda_D \omega_0)^{-1}\hat{v}_x$, $n = n_0^{-1}\hat{n}$, $f = (\lambda_D \omega_0/n_0)\hat{f}$, and $\varphi = (e/\kappa T)\hat{\varphi}$. By substituting these relations to Eqs. (35) and (36), we have the normalised Vlasov-Poisson system,

$$\partial_t f + v_x \partial_x f + \partial_x \varphi \partial_v f = 0, \tag{37}$$

$$-\partial_x^2 \varphi = 1 - \int f dv_x. \tag{38}$$

3.2 Basic principle of CIP scheme

Let us consider the following simple 1D hyperbolic equation,

$$\partial_t f + v \partial_x f = 0. \tag{39}$$

When v is constant, the analytic solution is given by

$$f(x, t + \Delta t) = f(x - v\Delta t, t). \tag{40}$$

Even if v is not constant, an approximate solution may be given by

$$f(x, t + \Delta t) \approx f(x - v\Delta t, t), \tag{41}$$

provided that Δt is small enough. Based on this idea, we integrate the time evolution of the propagation equation by shifting f. In this procedure, we need to compute interpolated values of f between discrete grids. The CIP method uses a Hermite interpolation defined by f_i and $(\partial f)_i$ at two neighbouring grid points. We write an approximate profile F_i between $x = x_i$ and $x = x_{iup}$ by a cubic polynomial function,

$$F_i(x = x_i + X) = A1_i X^3 + A2_i X^2 + A3_i X + A4_i, \tag{42}$$

where $iup = i + sgn(-v_i \Delta t)$. By imposing boundary conditions,

$$F_i(x_i) = f_i, \tag{43}$$

$$F_i(x_{iup}) = f_{iup}, \tag{44}$$

$$\partial_x F_i(x_i) = \partial_x f_i, \tag{45}$$

$$\partial_x F_i(x_{iup}) = \partial_x f_{iup}, \tag{46}$$

the coefficients $A1_i$, $A2_i$, $A3_i$, and $A4_i$ are determined as

$$A1_i = (\partial_x f_i + \partial_x f_{iup})/\delta^2 + 2(f_i - f_{iup})/\delta^3, \tag{47}$$

$$A2_i = -(2\partial_x f_i + \partial_x f_{iup})/\delta - 3(f_i - f_{iup})/\delta^2, \tag{48}$$

$$A3_i = \partial_x f_i, \tag{49}$$

$$A4_i = f_i, \tag{50}$$

where $\delta = x_{iup} - x_i$. In order to have boundary conditions (43)-(46), we propagate not only the value of f but also its gradient [2]. When v is independent of x, a propagation equation for $\partial_x f$ is obtained by differentiating Eq. (39),

$$\frac{\partial(\partial_x f)}{\partial t} + v\frac{\partial(\partial_x f)}{\partial x} = 0. \tag{51}$$

If we write $\xi = -v_i \Delta t$, the iteration process is given by

$$\begin{aligned} f_i^{n+1} &= F_i^n(x_i + \xi) \\ &= A1_i^n \xi^3 + A2_i^n \xi^2 + A3_i^n \xi + A4_i^n, \end{aligned} \tag{52}$$

where n indicates an index of iterations.

3.3 Basic principle of Lagrange interpolation scheme

Another simple way to interpolate f by a cubic polynomial function (42) is to use a Lagrange interpolation. When $sgn(-v_i \Delta t) = +1$, the boundary conditions at four successive grid points,

$$F_i(x_{i-1}) = f_{i-1}, \tag{53}$$

$$F_i(x_i) = f_i, \tag{54}$$

$$F_i(x_{i+1}) = f_{i+1}, \tag{55}$$

$$F_i(x_{i+2}) = f_{i+2}. \tag{56}$$

give the coefficients,

$$A1_i = (-f_{i-1} + 3f_i - 3f_{i+1} + f_{i+2})/6\delta^3, \tag{57}$$

$$A2_i = (f_{i-1} - 2f_i + f_{i+1})/2\delta^2, \tag{58}$$

$$A3_i = -(2f_{i-1} + 3f_i - 6f_{i+1} + f_{i+2})/6\delta, \tag{59}$$

$$A4_i = f_i. \tag{60}$$

The Lagrange interpolation scheme is advantageous because we do not need to compute $\partial_x f$. Its accuracy will be discussed in the next section.

3.4 Comparison of CIP and Lagrange interpolation schemes

In order to see numerical properties of interpolation schemes, we solve the 1D hyperbolic equation (39). In this test, we use N grid points to represent the x space with computational domain $0 \leq x < L$, and impose a periodic boundary condition $f(0) = f(L)$. The time step width is chosen as $\Delta t = (\delta/v)/8$ with the propagation speed $v = 1$.

Firstly, we solve the propagation of a sinusoidal wave given by the initial condition, $f(x) = \sin(2\pi x/L)$. In this test, numerical solutions obtained from both the CIP and Lagrange interpolation schemes are very close to analytic solution. We compare these numerical solutions with those obtained from the cubic spline interpolation method [5] [5] and from the linear interpolation scheme. Table I shows the relative integral error, $\sum_{i=1}^{N}(f_i - f_i^{analytic})/f_i^{analytic}$, observed after 100 iterations, where $f_i^{analytic}$ is the analytic solution. We see that the CIP scheme gives the best results for this kind of smooth curve.

We then simulate the propagation of a square wave. Figure 4 shows comparisons of numerical solutions after 100 iterations with the CIP, Lagrange interpolation, cubic spline interpolation, and linear interpolation schemes. In the results, the linear interpolation scheme shows very strong numerical diffusion compared to the other higher order schemes. Quantitative comparisons of the relative integral error are given in Table II. Again, the CIP scheme gives the best results. However, we must make a few warnings. Although the distribution function is positive in the initial condition, as shown in Fig.4, negative values appear after a few time steps, producing unphysical numerical oscillations. This also violates the monotonicity of the spatial derivative. Therefore, the scheme may not be valid for a profile with steep gradients or fine structures, and the grid size should be chosen small enough to resolve the finest scale in the system.

3.5 2D Vlasov CIP code

In extending the CIP code to 2D phase space (x-v_x), we use the method of fractional step [6]. Let us write Eq. (37) in phase space as a 2D hyperbolic equation in Cartesian coordinates (x, y),

$$\partial_t f + v_x \partial_x f + v_y \partial_y f = 0, \tag{61}$$

where $v_x(x, y) = y$ and $v_y(x, y) = e/m\partial_x \varphi$. In the fractional step technique, the integration of Eq. (61) is split into

$$\text{Step1}: \quad f_{ij}^{*} = L(x, \Delta t/2) f_{ij}^{n}, \tag{62}$$

$$\text{Step2}: \quad f_{ij}^{**} = L(y, \Delta t) f_{ij}^{*}, \tag{63}$$

$$\text{Step3}: \quad f_{ij}^{n+1} = L(x, \Delta t/2) f_{ij}^{**}, \tag{64}$$

where i, j are indices in the x- and y-directions, $n, n+1, *, **$ show solutions at the n-th, $n+1$-th, and intermediate steps, respectively, and $L(\lambda, \Delta t)$ gives the solution of equation $\partial_t f + v_\lambda \partial_\lambda f = 0$ after the time interval Δt. Since v_x (v_y) is independent of x (y)inEq.(61), each successive integration processes are written in conservative forms, $\partial_t f + \partial_\lambda v_\lambda f = 0$, and therefore, even after splitting approximation, conservation properties can be kept provided that a proper numerical scheme is chosen.

In applying the CIP scheme to Eq. (62) or

$$\partial_t f + v_x \partial_x f = 0, \tag{65}$$

we also need to advance $\partial_y f$ in addition to f and $\partial_x f$. By taking partial derivative in the y-direction, Eq. (65) yield an evolution equation for $\partial_y f$,

$$\partial_t(\partial_y f) + \partial_y(v_x \partial_x f) = 0. \tag{66}$$

In integrating Eq. (66), we use a simple centered finite difference approach,

$$\frac{\partial_y f^*_{ij} - \partial_y f^n_{ij}}{\Delta t} = -\frac{v_{x,j+1}\partial_x f^*_{i,j+1} - v_{x,j-1}\partial_x f^*_{i,j-1} + v_{x,j+1}\partial_x f^n_{i,j+1} - v_{x,j-1}\partial_x f^n_{i,j-1}}{4\Delta y}, \tag{67}$$

where $\partial_x f^*_{i,j}$ is calculated by an advection equation for $\partial_x f$. By replacing x and y, the same procedure is applicable also to Eq. (64). It is noted that this numerical procedure exactly conserves the total particle number [2].

In a Vlasov CIP code, we consider x-v_x phase space with computational domain $\{(x, v_x)|0 \le x < L, |v_x| \le v_{off}\}$. The grid numbers in the x- and v_x-directions are given by $n_x = L/\Delta x$ and $2n_{v_x} = 2v_{off}/\Delta v_x$, respectively, where Δx and Δv_x are grid spacing. The boundary conditions are periodic in the x-direction and fixed or $f(x, v_{off}) = 0$ in the v_x-direction. Before Step2, the electrostatic potential is calculated from the Poisson equation (38) using Fast Fourier Transform (FFT) technique [5].

3.6 Recurrence effect in free-streaming problem

Before showing simulations in the Vlasov-Poisson system, we solve a simple free-streaming problem without electric fields. This test is useful to understand a concept of phase mixing and how a recurrence effect occurs in solving the Vlasov equation based on a mesh approach. Let us compute the following free-streaming equation,

$$\partial_t f + v_x \partial_x f = 0, \tag{68}$$

which has an analytic solution given by $f(x, v_x, t) = f(x - v_x t, v_x, 0)$. The initial condition is $f(x, v_x, 0) = 1/\sqrt{2\pi}\exp(-v_x^2/2)A\cos(k_x x)$ and the parameters are $A = 0.01$, $k_x = 0.5$, $L = 4\pi$, $v_{off} = 5$, $n_x = 32$, $2n_{v_x} = 32$, and $\Delta t = 1/8$. It should be noted that although a distribution function with negative values has no physical meaning, we simulate this condition as a standard test case often discussed in earlier works [2, 6].

In a continuous system, the time history of the zeroth order moment ρ is estimated as

$$\begin{aligned}\rho(x,t) &= \int_{-\infty}^{+\infty} f(x, v_x, t)dv_x, \\ &= \int_{-\infty}^{+\infty} \frac{A}{\sqrt{2\pi}} e^{-v_x^2/2}\cos[k_x(x - v_x t)]dv_x, \\ &= Ae^{-k_x^2 t^2/2}\cos(k_x x), \end{aligned} \tag{69}$$

where the following relation is used,

$$\begin{aligned}\int_{-\infty}^{+\infty} \exp[-(v_x \pm \imath k_x t)^2/2]dv_x &= \int_{-\infty\pm\imath k_x t}^{+\infty\pm\imath k_x t} e^{-s^2/2}ds \\ &= \int_{-\infty}^{+\infty} e^{-s^2/2}ds \\ &= \sqrt{2\pi}. \end{aligned} \tag{70}$$

This solution shows that the density profile given at the initial time continuously decay in time, even though f is not damped. This decaying process comes from a property that fine structures produced by phase mixing are smeared out by integration over v_x.

On the other hand, in a discrete system, the time evolution of $\hat{\rho}$ is obtained as

$$\begin{aligned}\hat{\rho}(x,t) &= \sum_{j=-n_{v_x}}^{n_{v_x}-1} f(x, j\Delta v_x, t)\Delta v_x \\ &= \sum_{j=-n_{v_x}}^{n_{v_x}-1} \frac{A}{\sqrt{2\pi}} e^{-(j\Delta v_x)^2/2}\cos[k_x(x - j\Delta v_x t)]\Delta v_x. \end{aligned} \tag{71}$$

Here, we see that $\hat{\rho}$ is restored to its initial value after the recurrence time $T_R = 2\pi/(k_x\Delta v_x)$, because Eq. (71) satisfies $\hat{\rho}(x, pT_R) = \hat{\rho}(x, 0)$ for $p \in \mathbb{N}$. It is noted that in this work, we define the discrete velocity as $\hat{v}_x = (j + 1/2)\Delta v$. Because of this definition, the recurrence effect appear as $\hat{\rho}(x, 0) = -\hat{\rho}(x, T_R) = \hat{\rho}(x, 2T_R)$ in our system.

In the present case, the recurrence time is estimated as $T_R \sim 40.25$ ($it = 322$ iterations). This is clearly seen in Figs.5 and 6. In Fig.5, the numerical solution at $it = 150$ shows fine structures produced by phase mixing, and then, at $it = 322$, the numerical solution

is restored to $f(x, v_x, T_R) = -f(x, v_x, 0)$. Figure 6 shows the time ev olution of $|\rho|$. The numerical solution agree well with the analytic solution (70) up to $t \sim 9$. Then, the solution is deviated from its analytic solution, and the initial amplitude is reproduced at the recurrence time $t = T_R$. In order to see what is happening in phase space, we discuss the analytic solution in velocity wave number space k_v. We take k_v Fourier transform of the analytic solution,

$$\begin{aligned} f_{k_v}(x,t) &= \frac{1}{2\pi}\int_{-\infty}^{+\infty}\frac{1}{\sqrt{2\pi}}e^{-v_x^2/2}A\cos[k_x(x-v_xt)]e^{-\imath k_v v}dv \\ &= \frac{A}{4\pi}(e^{\imath k_x x}e^{-\frac{1}{2}(k_v+k_xt)^2} - e^{-\imath k_x x}e^{-\frac{1}{2}(k_v-k_xt)^2}). \end{aligned} \tag{72}$$

Figure 7 shows the time evolution of Eq. (72) at $x = 0$. In the plot, two wave packets propagate in opposite k_v directions, respectively, and at $t \sim 20$, they reach at the cut-off velocity wave number, which is defined as $k_{v,off} = \pm 2\pi n_{v_x}/(2v_{off}) \sim \pm 10$. Components beyond $k_{v,off}$ are reflected by aliasing [5], and the wave packets bounce back to reproduce the initial condition at $t = T_R \sim 40$. Since the recurrence effect comes from spurious k_v components produced by aliasing, it is completely unphysical. To avoid the recurrence effect, we must either stop the simulation before the recurrence effect occur, or increase the resolution in velocity space to extend the recurrence time.

4 NUMERICAL RESULTS

4.1 Conservations of particle number and energy

In order to examine the validity of the simulation, we check first principles such as the particle number conservation and the energy conservation. The Vlasov equation (37) can be written using the Hamiltonian h of a single particle motion,

$$\partial_t f + \partial_v h \partial_x f - \partial_x h \partial_v f = 0, \tag{73}$$

$$h = \frac{1}{2}v_x^2 - \varphi. \tag{74}$$

The conservation of the particle number $N(t)$ is obtained by integrating Eq. (73) over x and v_x,

$$\begin{aligned}\frac{dN}{dt} &= \int_0^{L_x}\int_{-\infty}^{\infty}\left[-\partial_v h\partial_x f + \partial_x h\partial_v f\right] dxdv_x \\ &= \int_0^{L_x}\int_{-\infty}^{\infty}\left[-\partial_x(\partial_v hf) + \partial_v(\partial_x hf)\right] dxdv_x \\ &= -\int_{-\infty}^{\infty}\left[\partial_v hf\right]_{x=0}^{x=L_x} dv_x + \int_0^{L_x}\left[\partial_x hf\right]_{v_x=-\infty}^{v_x=\infty} dx \\ &= 0, \end{aligned} \tag{75}$$

where the boundary conditions, $f(0, v_x, t) = f(L_x, v_x, t)$ and $f(x, -\infty, t) = f(x, \infty, t) = 0$, are used.

In a similar way, the energy conservation is derived by multiplying h to Eq. (73) and integrating it over x and v_x,

$$\begin{aligned}\int_0^{L_x}\int_{-\infty}^{\infty} h\partial_t f dxdv_x &= \int_0^{L_x}\int_{-\infty}^{\infty}\left[-h\partial_x(\partial_v hf) + h\partial_v(\partial_x hf)\right] dxdv_x \\ &= \int_0^{L_x}\int_{-\infty}^{\infty}\left[-\partial_x(h\partial_v hf) + \partial_v(h\partial_x hf)\right] dxdv_x \\ &= -\int_{-\infty}^{\infty}\left[h\partial_v hf\right]_{x=0}^{x=L_x} dv_x + \int_0^{L_x}\left[h\partial_x hf\right]_{v_x=-\infty}^{v_x=\infty} dx \\ &= 0. \end{aligned} \tag{76}$$

By substituting Eq. (74), Eq. (76) yields the total energy E_{tot}, the kinetic energy E_{kin}, and the field energy E_{fld},

$$\frac{dE_{tot}}{dt} = \frac{dE_{kin}}{dt} + \frac{dE_{fld}}{dt} = 0, \tag{77}$$

$$E_{kin} = \int_0^{L_x}\int_{-\infty}^{\infty}\left(\frac{1}{2}v_x^2 f\right) dxdv_x, \tag{78}$$

$$E_{fld} = \frac{1}{2}\int_0^{L_x}|\partial_x\varphi|^2 dx. \tag{79}$$

Figures 8 and 9 show the particle number conservation and the energy conservation observed in typical simulations of the Landau damping. In Fig.8, the breakdown of the particle number conservation is very small but finite. As discussed earlier, the present numerical scheme exactly conserves N. Therefore, a cause of the error of N comes from the boundary in the v_x-direction, where f is not zero. This can be seen by comparing simulations with different v_{off}. In Fig.8. the relative error of N is significantly reduced by extending

computational domain from $v_{off} = 4$ to $v_{off} = 5$. Figure 9 shows variations of the kinetic energy, the field energy, and the total energy. We observe that variations of the kinetic energy and the field energy are balanced with each other to ensure the energy conservation. In the present case, the error of the total energy is less than $\sim 10\%$ of the field energy and is $\sim 10^{-5}$ of the total energy.

4.2 Simulation of Landau damping

Let us compute the Landau damping by solving Eqs. (37) and (38) with the initial condition, $f(x, v_x, 0) = 1/\sqrt{2\pi}\exp(-v_x^2/2)[1 + A\cos(k_x x)]$. The simulation parameters are $A = 0.01$, $k_x = 0.5$, $L = 4\pi$, $v_{off} = 4$, $n_x = 32$, $2n_{v_x} = 32$, and $\Delta t = 1/8$. Here, a small amplitude of initial perturbations A provides a linear character of the problem.

Figure 10 shows the time history of the amplitude of the basic Fourier component ($k_x = 0.5$) of the electric field, $|E_k| = |k_x \varphi_k|$, and its comparison to the analytic solution. E_k decays exponentially in time as predicted by the theory of Landau damping, and the recurrence effect studied in the previous section occurs around the recurrence time $T_R \sim 48.7$. To evaluate ω_r and γ, we apply spectral analysis technique to the simulation data. Firstly, we extract the peaks by searching the data points which satisfy $dE_k/dt = 0$, and determine γ by applying the chi-square fitting [5] to these data points. We then remove the decrement component by multiplying E_k with $e^{\gamma t}$, apply a Welch window [5] to the data in order to reduce spurious leakage of the spectrum produced from finite time-series data with a square window, and perform FFT. Finally, we search for the peaks of the power spectrum to obtain ω_r. For the simulation in Fig.8, we get $\gamma = 0.1535$ and $\omega_r = 1.4223$, which are very close to the theoretical values [2], $\gamma_{th} = 0.1533$ and $\omega_{rth} = 1.4156$.

4.3 Comparison of numerical results with theory

We then compute the dispersion relation or the k_x-dependence of γ and ω_r from a systematic k_x scan. To perform this scan, we have to be careful about the simulation parameters, and they are chosen so that $k_x \Delta x < 1$, $T_R = 2\pi/(k_x \Delta v_x) = const.$, and $\omega_r \Delta t < 1$ or $k_x v_{off} \Delta t < 1$ are satisfied. Practically, we choose the standard simulation parameters as $k_x^0 = 0.5$, $\Delta_x^0 = \pi/8$, $\Delta_v^0 = 7.87 \times 10^{-2}$, and $\Delta t^0 = 1/8$, and then, determine parameters for

each k_x as $\Delta_x = c\Delta_x^0$, $\Delta_v = c\Delta_v^0$, and $\Delta t = c\Delta t^0$ ($\Delta t = \Delta t^0$ for $k_x < k_x^0$), where $c = k_x^0/k_x$. The other simulation parameters in the standard case are given as $L = 4\pi$, $v_{off} = 5$, $n_x = 32$, and $n_{v_x} = 128$. Comparisons of $\gamma(k_x)$ and $\omega_r(k_x)$ obtained from simulations and Eqs. (32) and (34) are shown in Fig.11. We see that numerical results agree very well with analytic estimation especially in a small k_x region, where the assumptions, $\xi \gg 1$ and $\gamma \ll \omega_r$, used in deriving Eqs. (32) and (34) are valid.

5 GENTLE-BUMP INSTABILITY

As an application of the analytic and numerical methods studied above, we study the stability of electrostatic waves in an electron plasma with a small bump in the tail of a Maxwellian distribution (see Fig.12). In this study, we consider the following equilibrium distribution function,

$$f_0(u) = n_M\sqrt{\frac{m}{2\pi\kappa T_M}}e^{-\frac{mu^2}{2\kappa T_M}} + n_B\sqrt{\frac{m}{2\pi\kappa T_B}}e^{-\frac{m(u-u_0)^2}{2\kappa T_B}}, \tag{80}$$

where the density of bulk and beam components, n_M and n_B, satisfy $n_M + n_B = n_0$ and $n_B \ll n_0$, the temperature of bulk and beam components, T_M and T_B, are assumed to be the same, $T_M = T_B$, and the beam drift velocity u_0 is given as $u_0 \gg v_{th}$.

5.1 Dispersion relation of gentle-bump instability

If we use the same assumptions as in Sec.2 , the dispersion relation (24) is given as

$$\begin{aligned} \mathfrak{Re}(D(\omega_r)) &= 1 + \frac{n_M}{\sqrt{\pi}k_x^2\lambda_D^2}\mathcal{P}\int\frac{ve^{-v^2}}{v-\xi}dv + \frac{n_B}{\sqrt{\pi}k_x^2\lambda_D^2}\mathcal{P}\int\frac{se^{-s^2}}{s-\chi}ds & (81)\\ &= 1 - \frac{n_M}{2k_x^2\lambda_D^2}Z'(\xi) - \frac{n_B}{2k_x^2\lambda_D^2}Z'(\chi), & (82)\end{aligned}$$

where $v = u/(\sqrt{2}v_{th})$, $s = (u-u_0)/(\sqrt{2}v_{th})$, $\xi = \omega_r/(\sqrt{2}k_x v_{th})$, and $\chi = (\omega_r/k_x - u_0)/(\sqrt{2}v_{th})$. In evaluating Z', we consider two limiting cases with different wave phase velocities $v_{ph} = \omega_r/k_x$. Firstly, when $v_{ph} \gg u_0 \gg v_{th}$, we can use the asymptotic forms of $Z(\xi)$ and $Z(\chi)$ under $\xi \gg 1$ and $\chi \gg 1$, respectively, and we have the same dispersion relations as the plasma oscillation given by Eq. (31). We denote two solutions shown in Eq. (32) by ω_+ and ω_-. On the other hand, when $v_{ph} \sim u_0 \gg v_{th}$, we approximate $Z(\chi)$ in the

limit of $\chi \sim 0$ by the following expansion[3],

$$Z(\chi) \sim -2\chi + \frac{4}{3}\chi^3 + \cdots . \tag{83}$$

By substituting Eqs. (30) and (83) to Eq. (82), we have the following dispersion relation,

$$1 - (1 - a_B)\frac{\omega_0^2}{\omega_r^2} + a_B \frac{1}{k_x^2 \lambda_D^2} = 0, \tag{84}$$

where $a_B = n_B/n_0$. We denote a solution of Eq. (84) as ω_1,

$$\omega_1 = \omega_0 \sqrt{\frac{1 - a_B}{1 + a_B/(k_x^2 \lambda_D^2)}}. \tag{85}$$

Figure 13 shows the three branches, ω_1, ω_+, and ω_-, and their domain of validity. We see that in a small k_x region, the three branches coexist.

We then estimate damping (growth) rates for these three branches. By substituting Eq. (80) to Eq. (33), we have an analytic expression of the damping rate,

$$\gamma(\omega_r) \sim \sqrt{\frac{\pi}{8}} \frac{\omega_r^3}{k_x^2 v_{th}^2} \left[(1 - a_B) \frac{\omega_r}{k_x v_{th}} e^{-\frac{1}{2}\left(\frac{\omega_r}{k_x v_{th}}\right)^2} + a_B \left(\frac{\omega_r}{k_x v_{th}} - \frac{u_0}{v_{th}} \right) e^{-\frac{1}{2}\left(\frac{\omega_r}{k_x v_{th}} - \frac{u_0}{v_{th}}\right)^2} \right]. \tag{86}$$

Eq. (86) shows that γ is determined by a balance between the first and second terms which come from bulk and beam components. While the first term is always stabilising, the second term changes its sign depending on v_{ph} and u_0, and it becomes a destabilising effect for $0 < v_{ph} < u_0$. By substituting Eqs. (32) and (85) to Eq. (86), we have three damping rates, $\gamma(\omega_1)$, $\gamma(\omega_+)$, and $\gamma(\omega_-)$. Since the ω_- branch is always stable, we discuss stability regimes of the ω_1 and ω_+ branches. Figure 14 shows the marginal stability curves given by $\gamma(\omega_1) = 0$ and $\gamma(\omega_+) = 0$ on the k_x-a_B plane and on the k_x-u_0 plane. From these parametric scans, we choose the simulation parameters of the gentle-bump instability as $u_0 = 4v_{th}$ and $a_B = 0.05$. In Fig.13, the damping rates of the ω_1 and ω_+ branches are plotted for these parameters. Although we see unstable k_x regions for both the ω_1 and ω_+ branches, the unstable k_x region of the latter branch is out of its validity limit.

5.2 Simulation of gentle-bump instability

In this section, we compare the above dispersion relation with numerical results obtained from the Vlasov CIP code. In the k_x scan of ω_r and γ of the gentle-bump instability, we use the same parameter set as used in Sec.4.

Figure 15 shows the k_x-dependence of the real frequency $\omega_r(k_x)$. For $k_x < 0.2$, two stable branches corresponding to ω_1 and ω_+ coexist. For $0.2 < k_x < 0.4$, we observe one unstable branch which has the real frequency in between the ω_1 and ω_+ branches. For $k_x > 0.4$, we find one stable branch near ω_+. Although the damping rate obtained from the simulation show a similar curve as that of the ω_1 branch in Fig.13, its unstable region is shifted to higher k_x. It is noted that the lowest order estimations of ω_+ and ω_1 in Eqs. (32) and (85) are not valid in this k_x region, because neither $\omega_r/k_x \gg u_0$ nor $\omega_r/k_x \sim u_0$ are satisfied for ω_+ and ω_1, respectively. Therefore, a direct computation of the dispersion relation (22) with the equilibrium distribution (80) is needed to have theoretical predictions for $k_x > 0.2$. In this work, we take a quasi-analytic approach where Eq. (86) is estimated using ω_r obtained from the simulation. Comparisons between the quasi-analytic estimations and the numerical results are shown in Fig.15. We see that the unstable k_x region is recovered by the quasi-analytic results. From this quasi-analytic estimation, we can also understand a transition from a single branch to two branches in a low k_x region. In the frequency spectrum of E_k, we observe only a single peak of the most unstable mode for $k_x > 0.2$, but around $k_x \sim 0.18$, we find two peaks corresponding to ω_1 and ω_+. As k_x decreases, a peak at ω_+ becomes dominant compared to that at ω_1. These features are consistent with a change of the most unstable or less stable mode from ω_1 to ω_+ at $k_x \sim 0.18$.

6 SUMMARY

In this work, we studied kinetic properties of small amplitude waves in an electron plasma described by the Vlasov-Poisson system using analytic and numerical approaches.

Firstly, starting from the 1D Vlasov-Poisson system, we solved the dispersion relation of plasma waves using Fourier-Laplace transform, and reviewed the theory of Landau damping. From this analysis, we had analytic estimations of the real frequency ω_r and the damping rate γ of plasma waves.

We then developed a Vlasov CIP code to solve the 1D Vlasov-Poisson system numerically. In this development, we examined numerical properties and accuracy of several numerical schemes by solving the propagation of sinusoidal and square waves, and adopted the CIP scheme. We confirmed the recurrence effect by solving a free-streaming problem, and discussed its mechanism by showing behaviours of the solution in the velocity wave number

space. In these numerical tests, we also discussed the validity limit of the simulation.

In order to test the physical validity of the Vlasov CIP code, we simulated Landau damping. In this simulation, firstly, we confirmed first principles such as the particle number conservation and the total energy conservation, and then, compared the numerical results with the analytic solution. The results showed that small amplitude ($\delta n/n_0 < 1\%$) and weakly damping ($\gamma/\omega_r \ll 1$) plasma waves were successfully simulated, and the dispersion relation was recovered with good accuracy. This proves the usefulness of the Vlasov CIP code in studying small-amplitude waves in a collisionless plasma.

Finally, we applied the above analytic and numerical approaches to the gentle-bump instability. The dispersion relation of plasma waves in an electron plasma with a beam component gives two branches in different regimes of the phase velocity ω_r/k_x. The analytic result predicts that in a low k_x region, two branches coexist, and that the transition of the most unstable or less stable mode from one branch to the other branch occurs with decreasing k_x. These complicated features of the gentle-bump instability was successfully captured by the Vlasov CIP code.

Although the present study focused on linear problems, in principle, the Vlasov CIP code can simulate their nonlinear evolutions. In future works, nonlinear problems will be addressed.

Acknowledgments

This work was performed as an internship work at JAEA from Jun. 2006 to Aug. 2006. The authors would like to thank Dr. T. Hirayama for his support on this internship program. The simulations were performed on the JAEA Origin300 system.

References

[1] L. Landau, "On the vibrations of the electronic plasma", *J. Phys. U.S.S.R.* **10**, 25 (1946).

[2] T. Nakamura and T. Yabe, "Cubic interpolated propagation scheme for solving the hyper-dimensional Vlasov-Poisson equation in phase space", *Comput. Phys. Commun.* **120**, 122 (1999).

[3] N. A. Krall and A. W. Trivelpiece, *Principles of plasma physics*, McGraw-Hill, New York (1973).

[4] H. W. Wyld, *Mathematical methods for physics*, Benjamin, New York (1976).

[5] W. H. Press, S. A. Teukolsky, W. T. Vetterling, and B. P. Flannery, *Numerical Recipes in Fortran 77, Second Edition*, Cambridge Univ. Press, Cambridge (1992).

[6] C. Z. Cheng and G. Knorr, "The integration of the Vlasov equation in configuration space", *J. Comput. Phys.* **22**, 330 (1976).

TABLE 1: The relative integral error after 100 iterations in propagation tests of a sinusoidal wave with grid numbers, $N = 100$ and $N = 200$.

$N \setminus$ Scheme	CIP	Lagrange	Spline	Linear
200	$2.33 \cdot 10^{-4}$ %	$1.53 \cdot 10^{-3}$ %	0.33 %	8.5 %
100	$3.6 \cdot 10^{-3}$ %	$2.4 \cdot 10^{-2}$ %	1.4 %	30 %

TABLE 2 : The relative integral error after 100 iterations in propagation tests of a square wave with grid numbers, $N = 100$ and $N = 200$.

$N \setminus$ Scheme	CIP	Lagrange	Spline	Linear
200	5.5 %	9.1 %	7.5 %	47 %
100	9.4 %	15.4 %	15.1 %	68 %

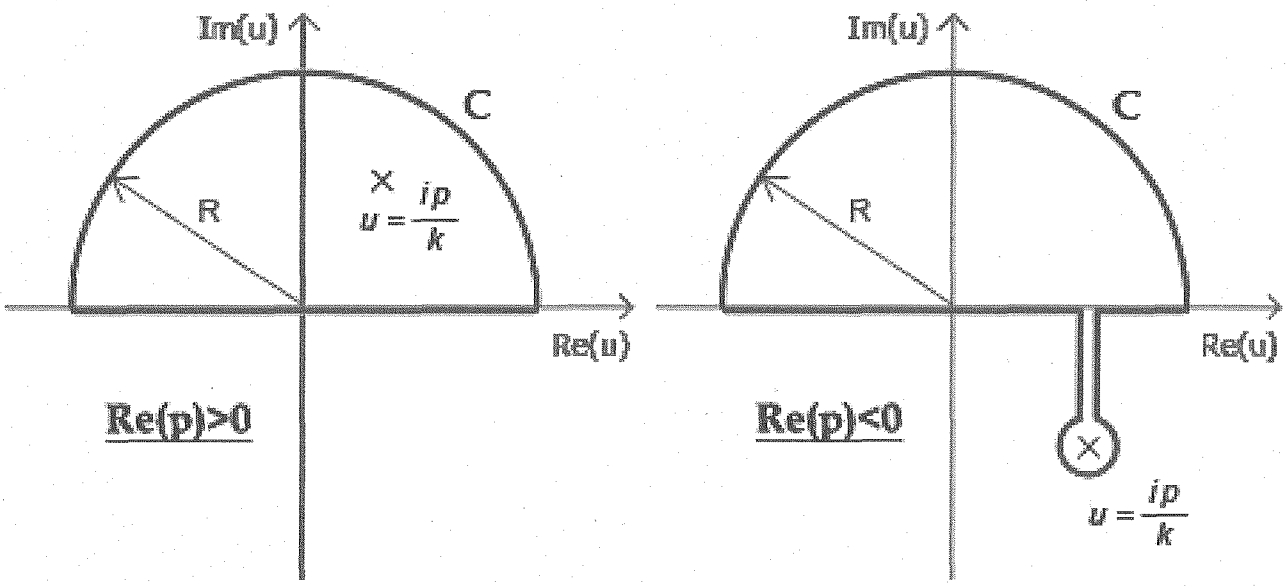

FIG. 1: Integration paths C with $\Re\mathrm{e}(p) > 0$ (left) and $\Re\mathrm{e}(p) < 0$ (right).

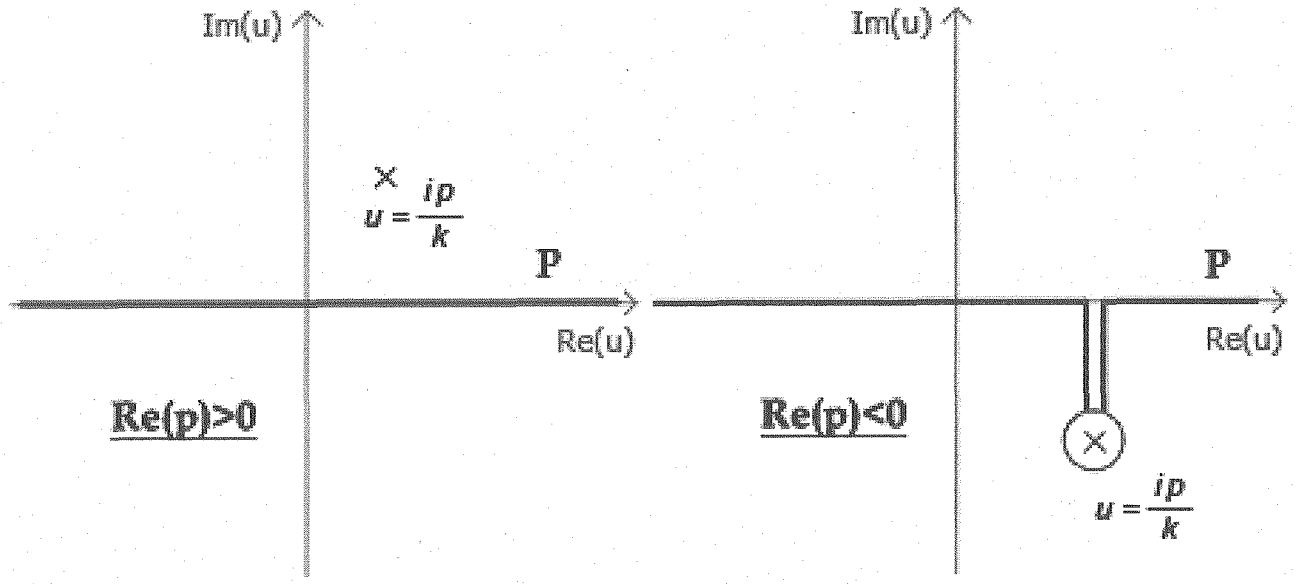

FIG. 2: Integration paths P used in the analytic continuation from $\Re e(p) > 0$ (left) to $\Re e(p) < 0$ (right).

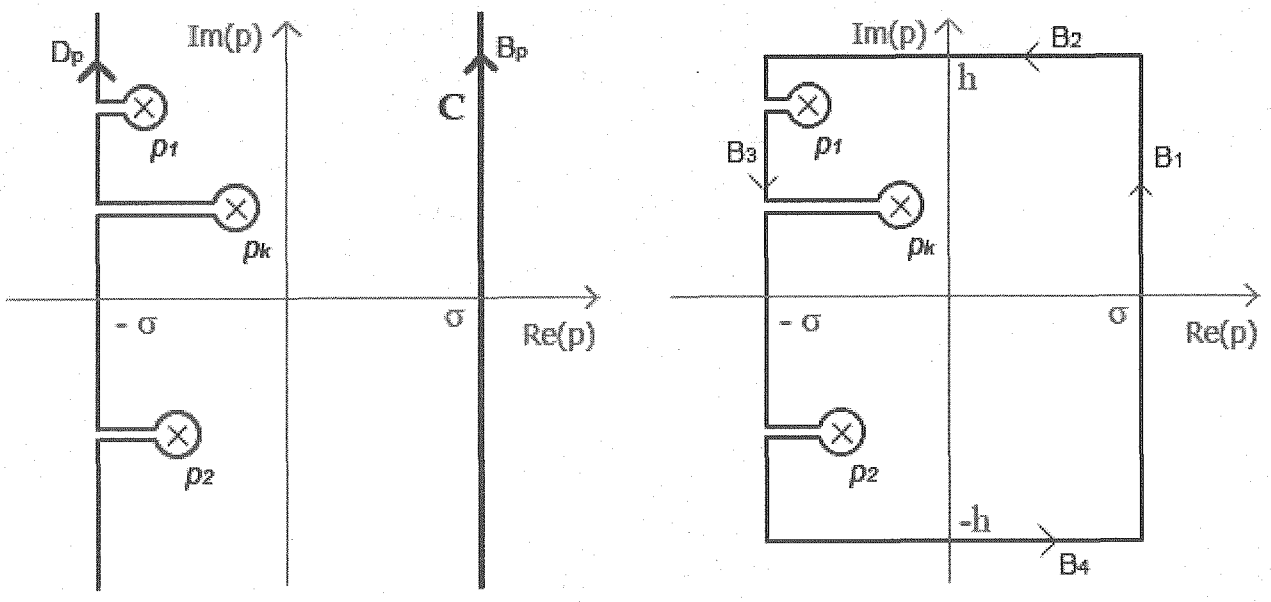

FIG. 3: The left figure shows Bromwitch path B_p and deformed path D_p. By considering auxiliary paths, equivalence between B_p and D_p can be seen (right).

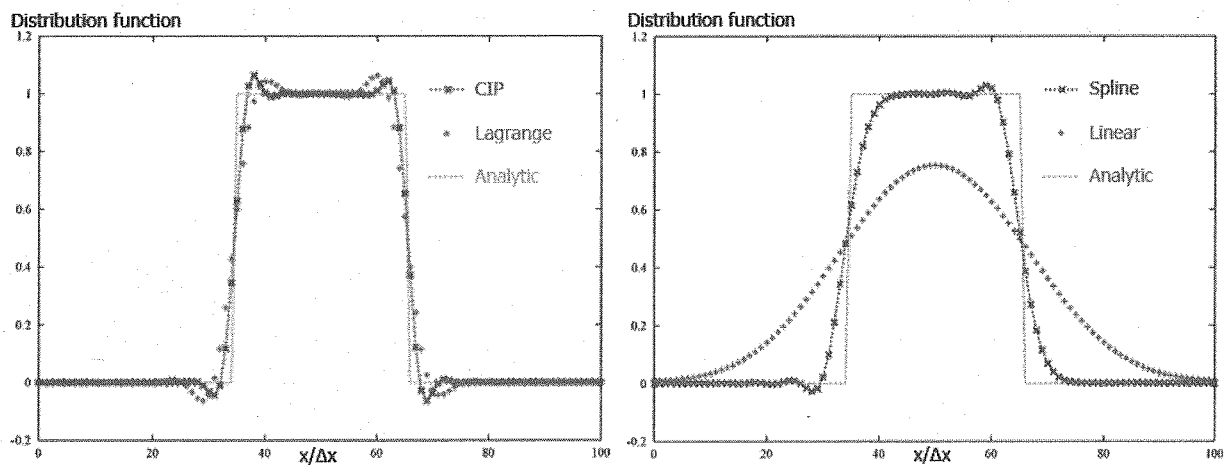

FIG. 4: The propagation of a square wave. Plots show comparisons of numerical solutions after 100 iterations.

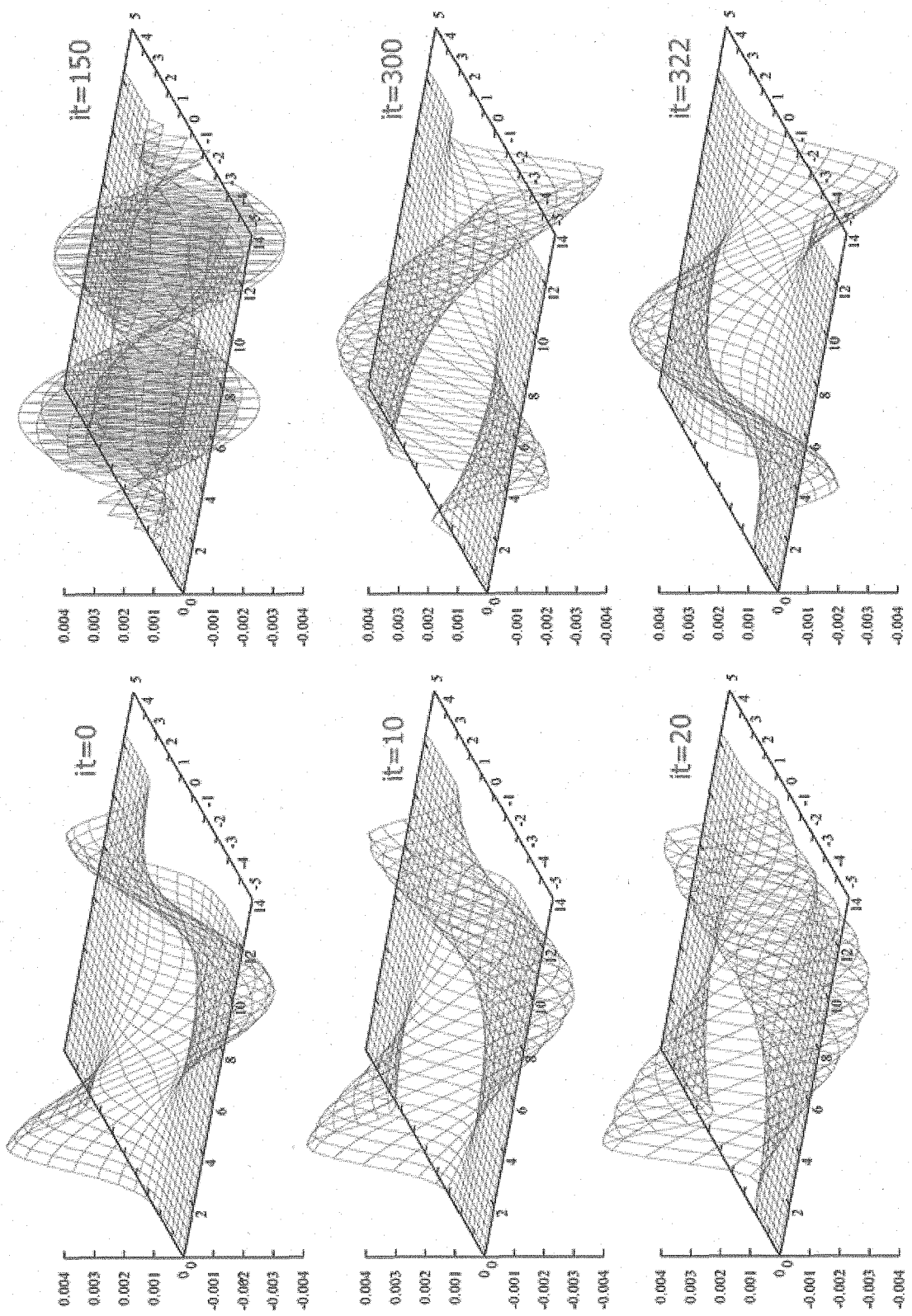

FIG. 5: The time evolutions of phase space structures of the distribution function in the free-streaming test.

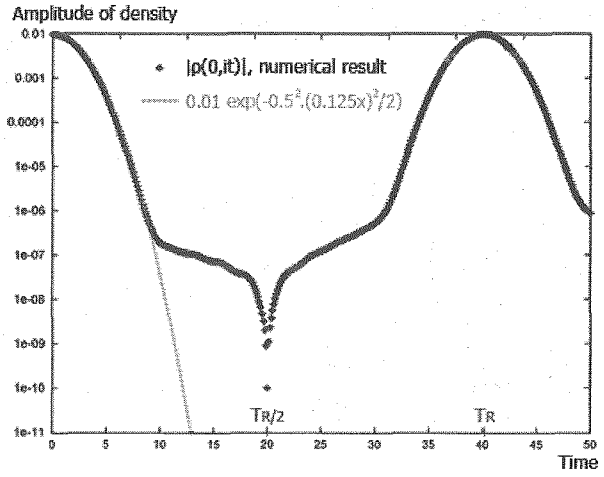

FIG. 6: A comparison between analytic and numerical solutions of ρ in the free streaming test. The initial amplitude of $|\rho|$ is recovered at the recurrence time $T_R \sim 40$.

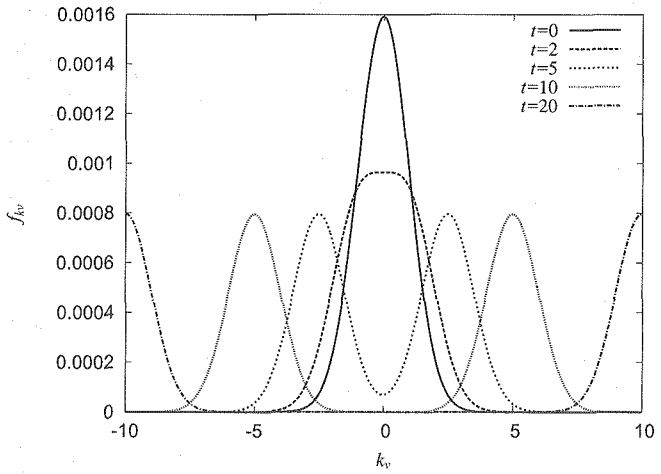

FIG. 7: The recurrence effect in velocity wave number space. The time evolutions of the analytic solution (72) is plotted at $x = 0$.

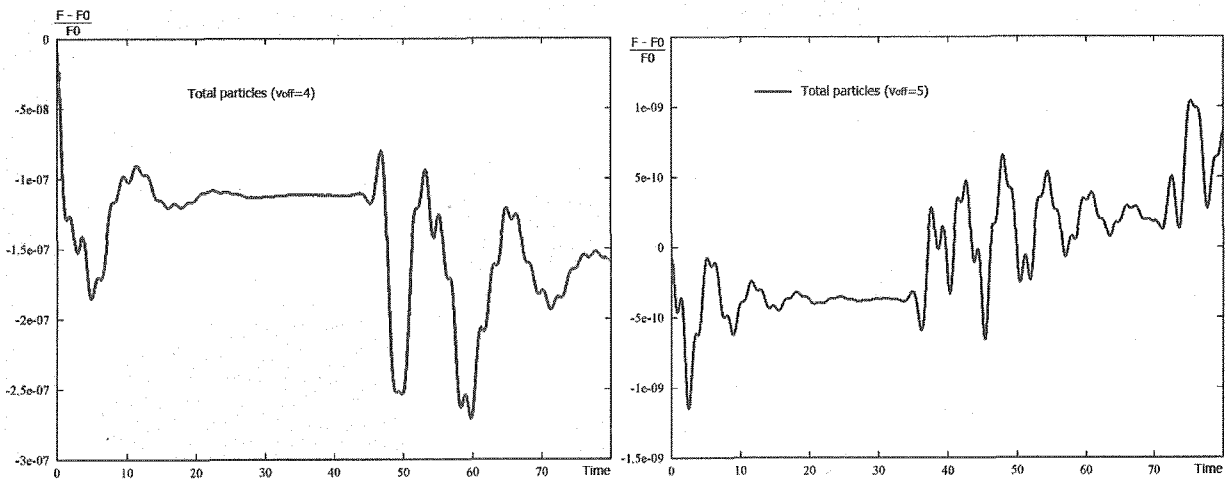

FIG. 8: The particle number conservation observed in a typical simulation of Landau damping with $v_{off} = 4$ (left) and $v_{off} = 5$ (right). The error of the particle number is significantly reduced by extending computational domain in the velocity space.

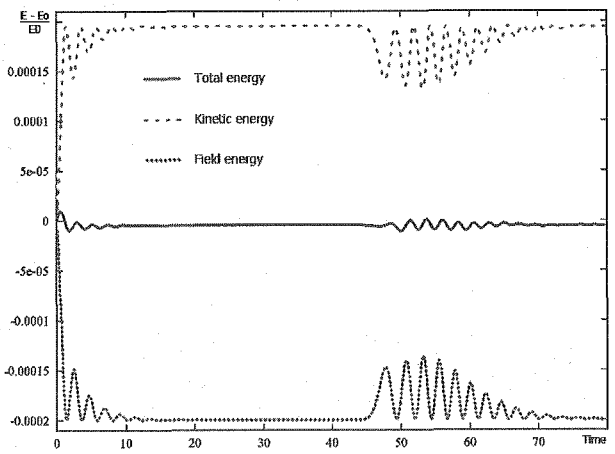

FIG. 9: The total energy conservation observed in the same simulation as Fig.8. In this simulation, the field energy absorbed by Landau damping goes to the kinetic energy to ensure the total energy conservation.

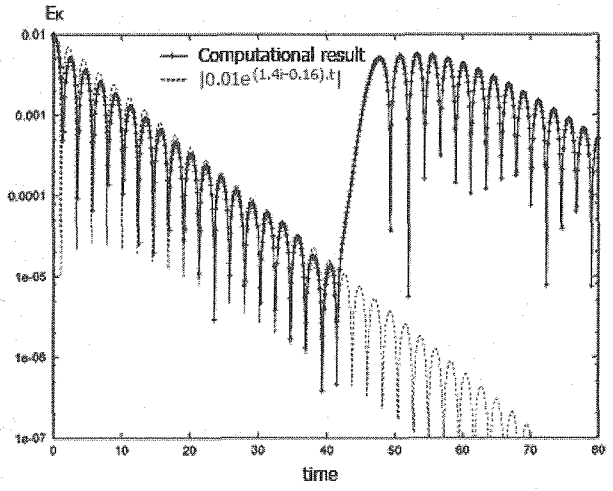

FIG. 10: The time history of the basic Fourier component of the electric field E_k observed in a typical simulation of Landau damping. The real frequency and the damping rate in the simulation result (red) agree well with a theoretical prediction (green). In the numerical result, the recurrence effect occurs at $T_R \sim 48$.

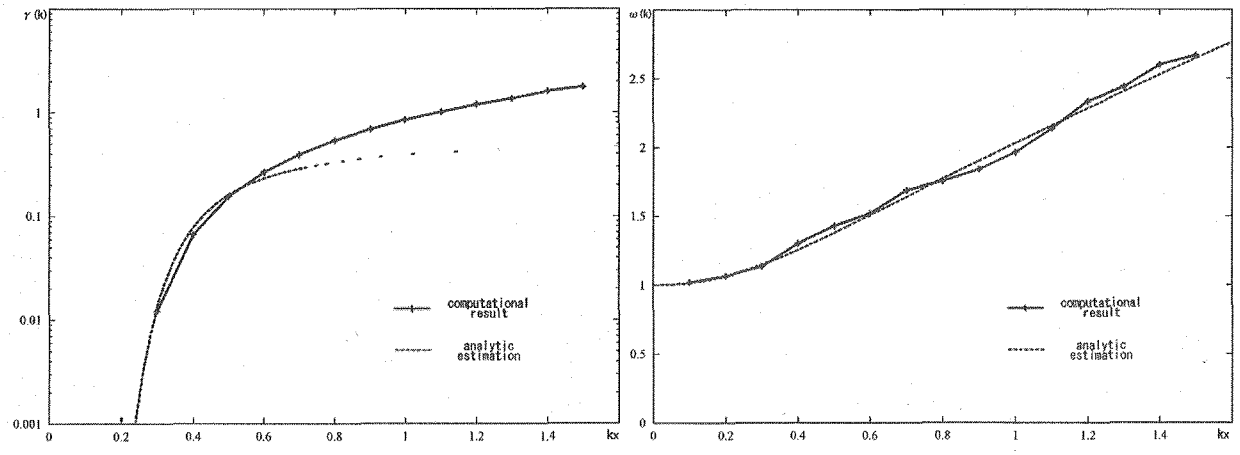

FIG. 11: Comparisons of numerical (red) and analytic (green) estimations of the damping rate γ (left) and the real frequency ω_r (right).

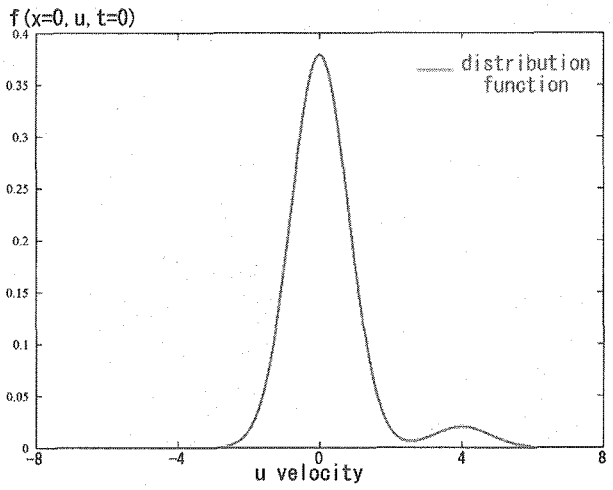

FIG. 12: The electron distribution function of a Maxwellian plasma with a beam component. Here, the beam drift velocity is $u_0 = 4v_{th}$.

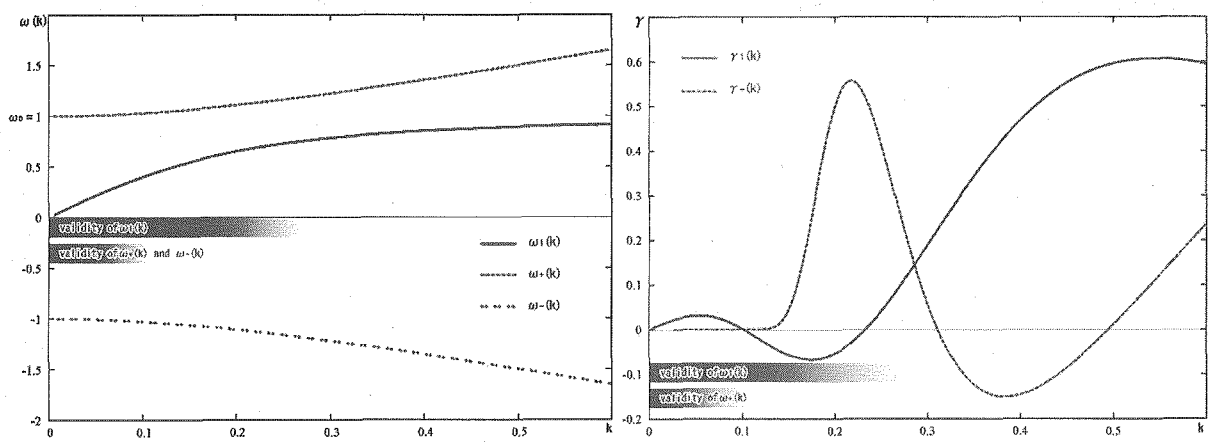

FIG. 13: The left figure shows real frequencies of ω_1, ω_+, and ω_- branches. The right figure is plots of damping rates of ω_1 and ω_+ branches. Parameters used are $u_0 = 4v_{th}$ and $a_B = 0.05$. In the plot, negative values mean an instability. Hatched regions denote domain of validity for assumptions $\chi \gg 1$ (green) and $\chi \sim 0$ (red) used in calculating ω_+ and ω_1.

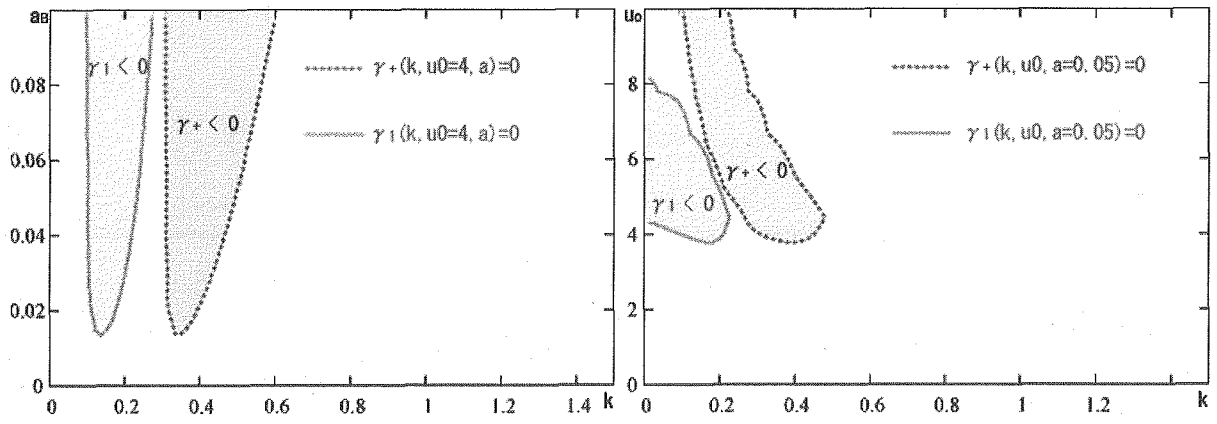

FIG. 14: k_x-a_B scan (left) and k_x-u_0 scan (right) of the stability diagram for ω_1 and ω_+ branches.

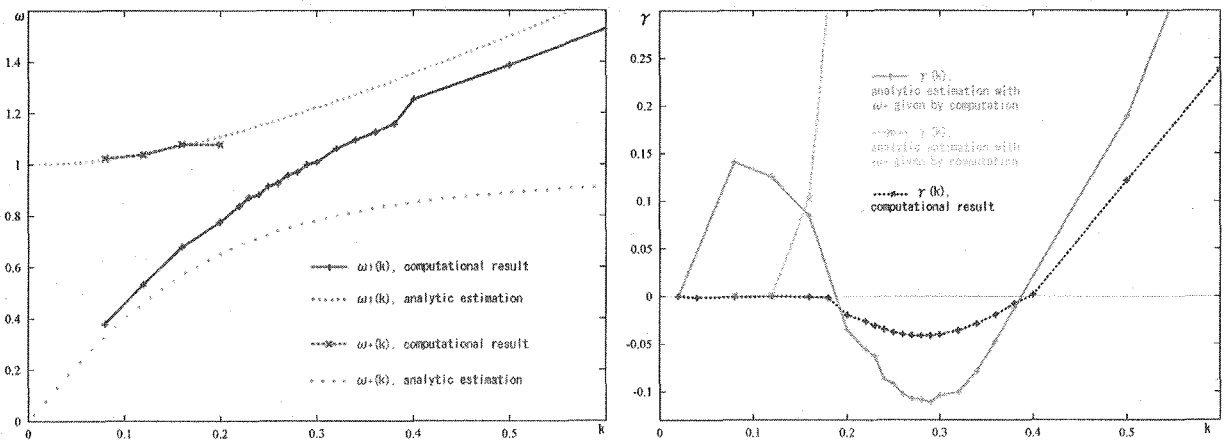

FIG. 15: The left figure shows a comparison of ω_r obtained from the simulation and from Eqs. (32) and (85). The right figure shows γ obtained from the simulation and from the quasi-analytic calculations using Eq. (86) and ω_r given by the simulation. Here, (+) symbols in gray, (×) symbols in gray, and (+) symbols in black are the quasi-analytic results with $\omega_1(k)$ and $\omega_+(k)$ in the left figure, and the simulations results, respectively

This is a blank page.

国際単位系（SI）

表１．SI 基本単位

基本量	SI 基本単位	
	名称	記号
長さ	メートル	m
質量	キログラム	kg
時間	秒	s
電流	アンペア	A
熱力学温度	ケルビン	K
物質量	モル	mol
光度	カンデラ	cd

表２．基本単位を用いて表されるSI組立単位の例

組立量	SI 基本単位	
	名称	記号
面積	平方メートル	m^2
体積	立法メートル	m^3
速さ，速度	メートル毎秒	m/s
加速度	メートル毎秒毎秒	m/s^2
波数	毎メートル	m^{-1}
密度（質量密度）	キログラム毎立法メートル	kg/m^3
質量体積（比体積）	立法メートル毎キログラム	m^3/kg
電流密度	アンペア毎平方メートル	A/m^2
磁界の強さ	アンペア毎メートル	A/m
（物質量の）濃度	モル毎立方メートル	mol/m^3
輝度	カンデラ毎平方メートル	cd/m^2
屈折率	（数の）1	1

表５．SI 接頭語

乗数	接頭語	記号	乗数	接頭語	記号
10^{24}	ヨタ	Y	10^{-1}	デシ	d
10^{21}	ゼタ	Z	10^{-2}	センチ	c
10^{18}	エクサ	E	10^{-3}	ミリ	m
10^{15}	ペタ	P	10^{-6}	マイクロ	μ
10^{12}	テラ	T	10^{-9}	ナノ	n
10^{9}	ギガ	G	10^{-12}	ピコ	p
10^{6}	メガ	M	10^{-15}	フェムト	f
10^{3}	キロ	k	10^{-18}	アト	a
10^{2}	ヘクト	h	10^{-21}	ゼプト	z
10^{1}	デカ	da	10^{-24}	ヨクト	y

表３．固有の名称とその独自の記号で表されるSI組立単位

組立量	SI 組立単位			
	名称	記号	他のSI単位による表し方	SI基本単位による表し方
平面角	ラジアン(a)	rad		$m \cdot m^{-1}=1$(b)
立体角	ステラジアン(a)	sr(c)		$m^2 \cdot m^{-2}=1$(b)
周波数	ヘルツ	Hz		s^{-1}
力	ニュートン	N		$m \cdot kg \cdot s^{-2}$
圧力，応力	パスカル	Pa	N/m^2	$m^{-1} \cdot kg \cdot s^{-2}$
エネルギー，仕事，熱量	ジュール	J	N・m	$m^2 \cdot kg \cdot s^{-2}$
工率，放射束	ワット	W	J/s	$m^2 \cdot kg \cdot s^{-3}$
電荷，電気量	クーロン	C		s・A
電位差（電圧），起電力	ボルト	V	W/A	$m^2 \cdot kg \cdot s^{-3} \cdot A^{-1}$
静電容量	ファラド	F	C/V	$m^{-2} \cdot kg^{-1} \cdot s^4 \cdot A^2$
電気抵抗	オーム	Ω	V/A	$m^2 \cdot kg \cdot s^{-3} \cdot A^{-2}$
コンダクタンス	ジーメンス	S	A/V	$m^{-2} \cdot kg^{-1} \cdot s^3 \cdot A^2$
磁束	ウエーバ	Wb	V・s	$m^2 \cdot kg \cdot s^{-2} \cdot A^{-1}$
磁束密度	テスラ	T	Wb/m^2	$kg \cdot s^{-2} \cdot A^{-1}$
インダクタンス	ヘンリー	H	Wb/A	$m^2 \cdot kg \cdot s^{-2} \cdot A^{-2}$
セルシウス温度	セルシウス度(d)	℃		K
光束	ルーメン	lm	cd・sr(c)	$m^2 \cdot m^{-2} \cdot cd=cd$
照度	ルクス	lx	lm/m^2	$m^2 \cdot m^{-4} \cdot cd=m^{-2} \cdot cd$
（放射性核種の）放射能	ベクレル	Bq		s^{-1}
吸収線量，質量エネルギー分与，カーマ	グレイ	Gy	J/kg	$m^2 \cdot s^{-2}$
線量当量，周辺線量当量，方向性線量当量，個人線量当量，組織線量当	シーベルト	Sv	J/kg	$m^2 \cdot s^{-2}$

(a)ラジアン及びステラジアンの使用は、同じ次元であっても異なった性質をもった量を区別するときの組立単位の表し方として利点がある。組立単位を形作るときのいくつかの用例は表４に示されている。
(b)実際には、使用する時には記号rad及びsrが用いられるが、習慣として組立単位としての記号“１”は明示されない。
(c)測光学では、ステラジアンの名称と記号srを単位の表し方の中にそのまま維持している。
(d)この単位は、例としてミリセルシウス度m℃のようにSI接頭語を伴って用いても良い。

表４．単位の中に固有の名称とその独自の記号を含むSI組立単位の例

組立量	SI 組立単位		
	名称	記号	SI 基本単位による表し方
粘度	パスカル秒	Pa・s	$m^{-1} \cdot kg \cdot s^{-1}$
力のモーメント	ニュートンメートル	N・m	$m^2 \cdot kg \cdot s^{-2}$
表面張力	ニュートン毎メートル	N/m	$kg \cdot s^{-2}$
角速度	ラジアン毎秒	rad/s	$m \cdot m^{-1} \cdot s^{-1}=s^{-1}$
角加速度	ラジアン毎平方秒	rad/s^2	$m \cdot m^{-1} \cdot s^{-2}=s^{-2}$
熱流密度，放射照度	ワット毎平方メートル	W/m^2	$kg \cdot s^{-3}$
熱容量，エントロピー	ジュール毎ケルビン	J/K	$m^2 \cdot kg \cdot s^{-2} \cdot K^{-1}$
質量熱容量（比熱容量），質量エントロピー	ジュール毎キログラム毎ケルビン	J/(kg・K)	$m^2 \cdot s^{-2} \cdot K^{-1}$
質量エネルギー（比エネルギー）	ジュール毎キログラム	J/kg	$m^2 \cdot s^{-2} \cdot K^{-1}$
熱伝導率	ワット毎メートル毎ケルビン	W/(m・K)	$m \cdot kg \cdot s^{-3} \cdot K^{-1}$
体積エネルギー	ジュール毎立方メートル	J/m^3	$m^{-1} \cdot kg \cdot s^{-2}$
電界の強さ	ボルト毎メートル	V/m	$m \cdot kg \cdot s^{-3} \cdot A^{-1}$
体積電荷	クーロン毎立方メートル	C/m^3	$m^{-3} \cdot s \cdot A$
電気変位	クーロン毎平方メートル	C/m^2	$m^{-2} \cdot s \cdot A$
誘電率	ファラド毎メートル	F/m	$m^{-3} \cdot kg^{-1} \cdot s^4 \cdot A^2$
透磁率	ヘンリー毎メートル	H/m	$m \cdot kg \cdot s^{-2} \cdot A^{-2}$
モルエネルギー	ジュール毎モル	J/mol	$m^2 \cdot kg \cdot s^{-2} \cdot mol^{-1}$
モルエントロピー，モル熱容量	ジュール毎モル毎ケルビン	J/(mol・K)	$m^2 \cdot kg \cdot s^{-2} \cdot K^{-1} \cdot mol^{-1}$
照射線量（X線及びγ線）	クーロン毎キログラム	C/kg	$kg^{-1} \cdot s \cdot A$
吸収線量率	グレイ毎秒	Gy/s	$m^2 \cdot s^{-3}$
放射強度	ワット毎ステラジアン	W/sr	$m^4 \cdot m^{-2} \cdot kg \cdot s^{-3}=m^2 \cdot kg \cdot s^{-3}$
放射輝度	ワット毎平方メートル毎ステラジアン	$W/(m^2 \cdot sr)$	$m^2 \cdot m^{-2} \cdot kg \cdot s^{-3}=kg \cdot s^{-3}$

表６．国際単位系と併用されるが国際単位系に属さない単位

名称	記号	SI 単位による値
分	min	1 min=60s
時	h	1h =60 min=3600 s
日	d	1 d=24 h=86400 s
度	°	1°=(π/180) rad
分	’	1’=(1/60)°=(π/10800) rad
秒	”	1”=(1/60)’=(π/648000) rad
リットル	l、L	1l=1 $dm^3=10^{-3}m^3$
トン	t	$1t=10^3$ kg
ネーパ	Np	1Np=1
ベル	B	1B=(1/2)ln10(Np)

表７．国際単位系と併用されこれに属さない単位でSI単位で表される数値が実験的に得られるもの

名称	記号	SI 単位であらわされる数値
電子ボルト	eV	$1eV=1.60217733(49) \times 10^{-19}J$
統一原子質量単位	u	$1u=1.6605402(10) \times 10^{-27}kg$
天文単位	ua	$1ua=1.49597870691(30) \times 10^{11}m$

表８．国際単位系に属さないが国際単位系と併用されるその他の単位

名称	記号	SI 単位であらわされる数値
海里		1海里=1852m
ノット		1ノット=1海里毎時=(1852/3600)m/s
アール	a	$1a=1\ dam^2=10^2m^2$
ヘクタール	ha	$1ha=1\ hm^2=10^4m^2$
バール	bar	1 bar=0.1MPa=100kPa=1000hPa=10^5Pa
オングストローム	Å	$1Å=0.1nm=10^{-10}m$
バーン	b	$1b=100fm^2=10^{-28}m^2$

表９．固有の名称を含むCGS組立単位

名称	記号	SI 単位であらわされる数値
エルグ	erg	$1\ erg=10^{-7}$ J
ダイン	dyn	$1\ dyn=10^{-5}$N
ポアズ	P	$1\ P=1\ dyn \cdot s/cm^2=0.1Pa \cdot s$
ストークス	St	$1\ St=1cm^2/s=10^{-4}m^2/s$
ガウス	G	1 G ^10^{-4}T
エルステッド	Oe	1 Oe ^(1000/4π)A/m
マクスウェル	Mx	1 Mx ^10^{-8}Wb
スチルブ	sb	$1\ sb=1cd/cm^2=10^4cd/m^2$
ホト	ph	$1\ ph=10^4lx$
ガル	Gal	$1\ Gal=1cm/s^2=10^{-2}m/s^2$

表10．国際単位に属さないその他の単位の例

名称	記号	SI 単位であらわされる数値
キュリー	Ci	$1\ Ci=3.7 \times 10^{10}Bq$
レントゲン	R	$1\ R=2.58 \times 10^{-4}C/kg$
ラド	rad	$1\ rad=1cGy=10^{-2}Gy$
レム	rem	$1\ rem=1\ cSv=10^{-2}Sv$
X線単位		$1X\ unit=1.002 \times 10^{-4}nm$
ガンマ	γ	$1\gamma=1\ nT=10^{-9}T$
ジャンスキー	Jy	$1\ Jy=10^{-26}W \cdot m^{-2} \cdot Hz^{-1}$
フェルミ		$1\ fermi=1\ fm=10^{-15}m$
メートル系カラット		1 metric carat = 200 mg = 2×10^{-4}kg
トル	Torr	1 Torr = (101 325/760) Pa
標準大気圧	atm	1 atm = 101 325 Pa
カロリー	cal	
ミクロン	μ	$1\ \mu=1\mu m=10^{-6}m$

（第７版，1998年改訂）